

## ARTICLE OPEN



# Micro-electrochemical insights into pit initiation site on aged UNS S32750 super duplex stainless steel

Shuichiro Amatsuka<sup>1</sup>, Masashi Nishimoto<sup>1</sup>, Izumi Muto<sup>1</sup>, Makoto Kawamori<sup>2</sup>, Yuya Takara<sup>2</sup> and Yu Sugawara<sup>1</sup>

An aging treatment of UNS S32750 super duplex stainless steel at 1173 K for 1.0 ks produced  $\sigma$  and secondary austenite ( $\gamma_2$ ) phases in the  $\alpha$  and  $\gamma$  phase boundary regions. Small amount of Mn-Cr oxide and MnS complex inclusions were present in the steel. No pitting was observed during the potentiodynamic polarization of a small area ( $200 \times 200 \mu\text{m}$ ) without inclusions in 1 M  $\text{MgCl}_2$  at 348 K. Because the electrode area included  $\alpha$ ,  $\gamma$ ,  $\sigma$ , and  $\gamma_2$  phases, these phases and their boundaries alone could not act as initiation sites for pitting. The electrode area size was gradually reduced from  $3 \times 3 \text{ mm}$  to  $1 \times 1 \text{ mm}$ , and pitting corrosion was observed to occur at the Mn-Cr oxide and MnS complex inclusions in a region that appeared to be the  $\gamma_2$  phase near the  $\sigma$  phase.

npj Materials Degradation (2023)7:15; <https://doi.org/10.1038/s41529-023-00335-8>

## INTRODUCTION

Stainless steels are fundamental materials for a sustainable society, and attempts are being made to improve their corrosion resistance<sup>1,2</sup>. Duplex stainless steels contain an approximate 1:1 ratio of ferrite ( $\alpha$ ) and austenite ( $\gamma$ ) phases, and have attracted attention because of their superior mechanical properties and corrosion resistance<sup>3</sup>. The  $\gamma$  phase is sometimes called the primary  $\gamma$  phase to distinguish it from the secondary austenite ( $\gamma_2$ ) phase produced during the sigma ( $\sigma$ ) phase formation by the eutectoid reaction ( $\alpha \rightarrow \sigma + \gamma_2$ )<sup>4</sup>. However, in this study, it is simply referred to as the  $\gamma$  phase. Super duplex stainless steels, which generally contain approximately 25 mass% Cr, up to 4 mass% Mo, and up to 0.3 mass% N, exhibit extremely high pitting corrosion resistance in chloride solutions, as compared to traditional duplex stainless steels<sup>5,6</sup>. UNS S32750 (Fe-25Cr-7Ni-4Mo-0.28N) is one of the most widely used super duplex stainless steels owing to its high strength and toughness with adequate weldability, and further applications are expected in the future<sup>7</sup>.

Because UNS S32750 is a highly alloyed steel, it is prone to the formation of secondary phases, such as the  $\sigma$  phase, during heat treatment and the pitting corrosion resistance decreases mainly due to the  $\sigma$  phase precipitation<sup>8-11</sup>. According to the UNS S32750 time-temperature-precipitation (TTP) diagrams, the  $\sigma$  phase precipitates within a few minutes at approximately 1200 K<sup>12</sup>. Therefore, suppressing  $\sigma$  phase precipitation is difficult without rapid cooling. Welding and hot forming generally produce the  $\sigma$  phase, thereby reducing the pitting corrosion resistance. Moon *et al.* studied the effects of heat treatment on the pitting corrosion resistance of UNS S32750 welds<sup>10</sup>. They confirmed  $\sigma$  phase precipitation in the welds and reported that pitting corrosion occurred at the  $\sigma/\alpha$  and  $\sigma/\gamma$  phase boundaries. In duplex stainless steels, the  $\sigma$  phase generally precipitates at the  $\alpha/\gamma$  phase boundaries<sup>13-21</sup>. Therefore, pitting corrosion on duplex stainless steels usually occurs in the boundary regions of the  $\alpha$  and  $\gamma$  phases when the  $\sigma$  phase precipitates<sup>21-26</sup>.

It is well known that the  $\sigma$  phase is rich in Cr and Mo and low in Ni; hence, the depletion of Cr and Mo occurs around the  $\sigma$  phases. Thus, most corrosion studies of duplex stainless steels focus on the electrochemical properties in the vicinity of the  $\sigma$  phases<sup>27-33</sup>.

Park *et al.* conducted electrochemical noise analysis and reported that  $\sigma$  phase precipitation depletes Cr and Mo at and around the  $\sigma/\alpha$  and  $\sigma/\gamma$  boundaries. They considered that  $\sigma$  phase precipitation repeatedly causes de-passivation and re-passivation, thereby leading to pitting in the  $\alpha/\gamma$  phase boundary regions<sup>33</sup>. Because Cr and Mo are essential elements for the pitting corrosion resistance of super duplex stainless steels, the depletion of Cr and Mo is a critical factor for pit initiation. However, it is unlikely that UNS S32750 with 25 mass% Cr and 4 mass% Mo would undergo severe depletion and that de-passivation readily occurs in chloride solutions at a near-neutral pH. Park and Karlsson showed that pitting corrosion is initiated in the  $\gamma_2$  phase, which are formed by the eutectoid reaction in the  $\alpha$  and  $\gamma$  phase boundary region. They proposed that pitting occurs in the  $\gamma_2$  phases because of the low Cr and Mo amounts<sup>27</sup>. The formation of the  $\gamma_2$  phase can explain the increase in susceptibility to pitting because of the  $\sigma$  phase precipitation, and many similar proposals have been made<sup>28-32</sup>. However, the Cr and Mo contents in the  $\gamma_2$  phase of UNS S32750 aged at approximately 1150 K for 60–100 min is reported to be approximately 25 and 2.5 mass%, respectively<sup>34,35</sup>. Zhang *et al.* reported that the Cr and Mo contents in the  $\gamma_2$  phase of UNS S32707 (Fe-27Cr-7Ni-4.8Mo-1Cu-0.4N) were 24 and 3 mass%, respectively, even when it was aged for 100 min at the nose temperature in the TTP curve of the  $\sigma$  phase precipitation<sup>36</sup>. Unlike the sensitization of Fe-18Cr-8Ni austenitic stainless steel, the low Cr and Mo contents alone may not be sufficient to explain why the  $\gamma_2$  phase acts as the initiation site for pitting.

Nonmetallic inclusions, such as MnS inclusions, are known to be initiation sites for pitting on austenitic, ferritic, and martensitic stainless steels in chloride solutions<sup>37-47</sup>. It has also been highlighted that duplex stainless steels may play an important role in pit initiation<sup>48-50</sup>. Garfias and Siconolfi found precursor sites for pitting corrosion in duplex stainless steels using a modified near-field scanning optical microscope<sup>48</sup>. They demonstrated that pits are initiated at inclusions in UNS S32550 (Fe-26Cr-6Ni-3Mo-2Cu-0.2N). The inclusions were analyzed and found to be inhomogeneous and consisting of a mixture of various elements (Si, Al, Mg, Ca, Ti, Mn, and S). Yang *et al.* studied the effect of heat input on the microstructure and corrosion behavior of UNS31803 (Fe-22Cr-5Ni-3Mo-0.15N) in 3.5% NaCl<sup>49</sup>.

<sup>1</sup>Department of Materials Science, Graduate School of Engineering, Tohoku University, 6-6-02, Aza-Aoba, Aramaki, Aoba-ku, Sendai 980-8579, Japan. <sup>2</sup>Kobe Corporate Research Laboratories, Kobe Steel, Ltd., 5-5, Takatsukadai 1-chome, Nishi-ku, Kobe, Hyogo 651-2271, Japan. ✉email: shuichiro.amatsuka.p3@dc.tohoku.ac.jp; mutoi@material.tohoku.ac.jp

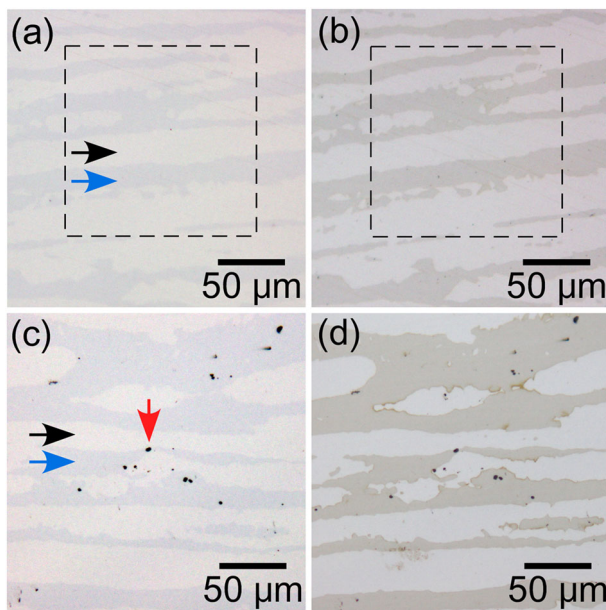
After anodic polarization, they observed pits in which very small amounts of inclusions consisting of O-Mn-Al-Si-Ca were observed. Zhang et al. investigated the relationship between the microstructure and pitting corrosion behavior of UNS S32750 welds after a short heat treatment<sup>50</sup>. They demonstrated that pits were readily initiated at oxide mixed inclusions (Al, Si, and Ca) in the  $\alpha$  phases of the as-welded heat-affected zone. However, no studies have analyzed the relationship between the  $\gamma_2$  phase formation and inclusions in the pitting corrosion initiation of UNS S32750 super duplex stainless steel.

In this study, small working electrode areas with and without inclusions were fabricated on aged UNS S32750 super duplex stainless steel, and potentiodynamic polarization was performed in a chloride solution. And, the size of the electrode area was gradually reduced to identify the pitting corrosion initiation site, and the roles of the  $\gamma_2$  phase and inclusions in pit initiation were determined.

## RESULTS AND DISCUSSION

### Microstructural characterization

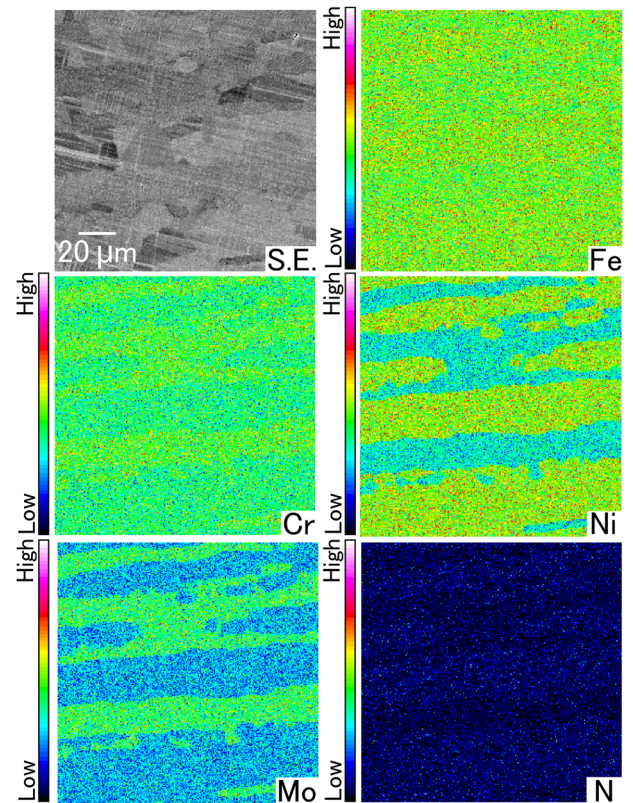
Figure 1a shows an optical micrograph of the as-polished surface of the solution-treated UNS S32750. Elongated gray and white areas were faintly visible. One of the gray areas is indicated by a blue arrow, and one of the white areas is indicated by a black arrow. As seen in Fig. 1c, inclusions were present in the steel. One of these is indicated by a red arrow in Fig. 1c. Inclusions were confirmed to exist in both the white and gray areas, and some existed at the boundaries between them. Figure 1b shows an optical micrograph of the solution-treated specimen etched using Murakami solution. The image in Fig. 1b is at the same position as that presented in Fig. 1a. The gray areas in Fig. 1a are the darker gray areas slightly discolored brown in Fig. 1b. In contrast, the white areas were barely discolored. Etching was also performed on the area shown in Fig. 1c, and the same discoloration as in Fig. 1b were confirmed, as presented in Fig. 1d. When duplex stainless steels are etched with Murakami solution, the  $\alpha$  phase discolors but no discoloration occurs in the  $\gamma$  phase<sup>51,52</sup>. Therefore, the gray and white areas are the  $\alpha$  and  $\gamma$  phases, respectively.



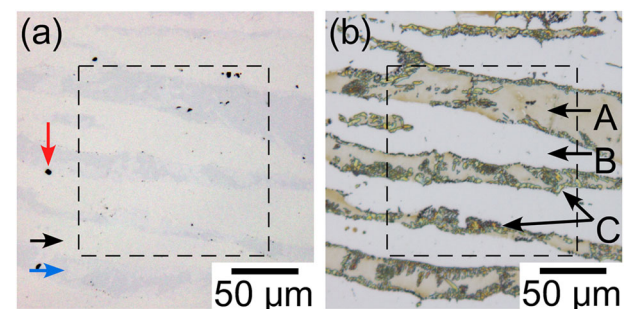
**Fig. 1** Optical micrographs of the solution-treated specimen. **a, b** Area with few inclusions and **c, d** area with inclusions: **a, c** as-polished and **b, d** after etching.

Figure 2 shows a SEM image and EPMA maps of the solution-treated specimens. This observation was conducted in the area demarcated by the dashed broken square in Fig. 1. The EPMA maps show that the Cr and Mo intensities in the gray areas were higher than those in the white areas. In contrast, the intensity of Ni in the white areas was higher than that in the gray areas. For duplex stainless steels, the Cr and Mo contents in the  $\alpha$  phase are higher than those in the  $\gamma$  phase, and the Ni content in the  $\gamma$  phase is higher than that in the  $\alpha$  phase. Therefore, Fig. 2 clearly indicates that the gray and white areas were  $\alpha$  and  $\gamma$  phases, respectively. These results also confirmed that the Murakami solution clearly distinguished the  $\alpha$  and  $\gamma$  phases of the super duplex stainless steel used in this study.

Figure 3a shows an optical micrograph of the as-polished surface of the aged UNS S32750. White and dark areas were faintly visible and the existence of inclusions was confirmed. The red arrow in Fig. 3a indicates an inclusion, which was located at the



**Fig. 2** SEM image and EPMA maps of the solution-treated specimen. The observation was conducted in the area demarcated by the dashed broken square in Fig. 1.



**Fig. 3** Optical micrographs of the aged specimen. **a** As-polished and **b** after etching. An area with inclusions was photographed.

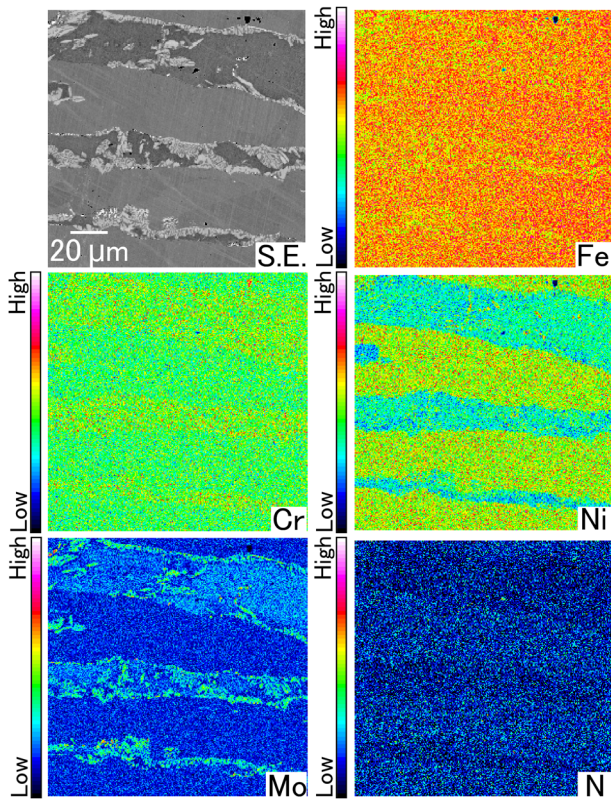


**Fig. 4 SEM image and EPMA maps of the aged specimen.** The observed and analyzed area was that demarcated by the dashed black square in Fig. 3.

boundary between the white and gray areas. Inclusions also existed in the white and gray areas. Figure 3b shows an optical micrograph of the aged specimen after etching with Murakami solution. The image in Fig. 3b was captured at the same position as that in Fig. 3a. In this figure, three different areas were observed, namely (1) brown, (2) white, and (3) bluish dark-gray areas, which were labeled as A, B, and C, respectively. The brown and white areas correspond to the  $\alpha$  and  $\gamma$  phases, respectively. No bluish dark-gray areas were observed in the solution-treated specimen (Fig. 1b). Therefore, the bluish dark-gray areas were generated during the aging treatment. Interestingly, most of the bluish dark-gray areas were observed along the boundaries between the  $\alpha$  and  $\gamma$  phases, appearing inside the  $\alpha$  phases (brown areas).

Figure 4 shows a SEM image and the corresponding EPMA maps of the aged specimen. The observed and analyzed area was that demarcated by the dashed black square in Fig. 3. The brown areas in Fig. 3 were rich in Cr and Mo. In contrast, the white areas were rich in Ni. These observations correspond to that in the solution-treated specimen; therefore, the brown and white areas are  $\alpha$  and  $\gamma$  phases, respectively. The intensity of Cr in the bluish dark-gray areas was almost the same as that of the  $\alpha$  phase; however, the intensity of Mo was exceptionally high, suggesting that the bluish dark-gray areas are  $\sigma$  phases, which are known to be precipitated during aging treatment<sup>3–6</sup>. The  $\sigma$  phase precipitates at the  $\alpha$  and  $\gamma$  phase boundary, and is known to grow toward the inside of the  $\alpha$  phase<sup>13–21</sup>. To identify the bluish dark-gray areas, STEM analysis was conducted.

To prepare the STEM specimen, the aged specimen was etched using Murakami solution. Figure 5a shows an optical microscopy image of an  $\alpha$  and  $\gamma$  phase boundary region of the specimen. In this image, a  $\gamma$  phase (white area) is present on the left side and an

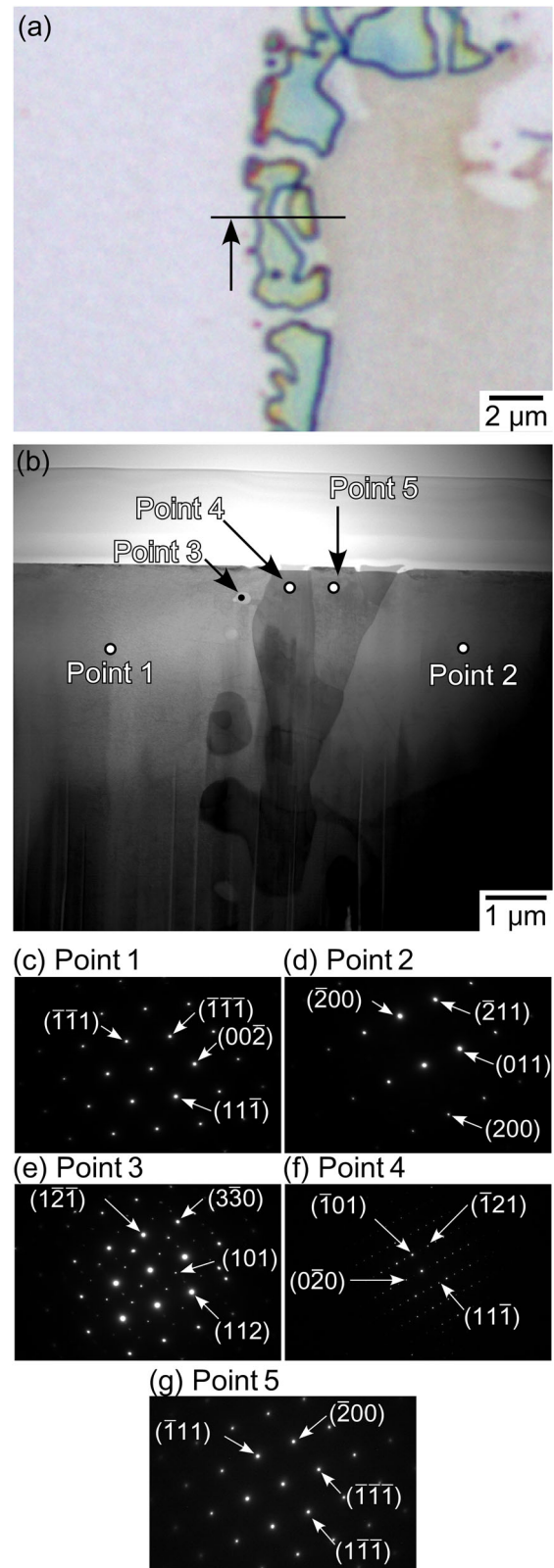


**Fig. 5 An  $\alpha$  and  $\gamma$  phase boundary region of the aged specimen.** **a** Optical micrograph of a boundary between the  $\alpha$  and  $\gamma$  phases of the aged specimen after etching. **b** STEM bright field image of the cross-section along the black line shown in **a**. STEM observation was made from the direction of the arrow in **a**. **c–g** Electron diffraction patterns at **c** Point 1, **d** Point 2, **e** Point 3, **f** Point 4, and **g** Point 5 shown in **b**.

$\alpha$  phase (brown area) is present on the right side. Furthermore, blue areas were visible between the  $\alpha$  and  $\gamma$  phases. The blue areas in this image correspond to the bluish dark-gray areas shown in Fig. 3b. An FIB lift-out specimen was fabricated along the black line shown in Fig. 5a, and STEM observations were performed from the direction of the black arrow in Fig. 5a.

Figure 5b shows a STEM bright-field image of the FIB lift-out specimen. Electron diffraction patterns were obtained, and an EDS point analysis was performed to identify the phases at Points 1–5. Figures 5c–g show the diffraction patterns at Points 1–5 and Table II presents the EDS analysis results. For reference, the line analysis results are shown in Supplementary Fig. 1. Based on the diffraction selection rules for BCC and FCC, it was determined that the crystal structures at Point 1 (Fig. 5c) and Point 2 (Fig. 5d) were FCC ( $\gamma$  phase) and BCC ( $\alpha$  phase), respectively. As shown in Table 1, the Cr concentration at Point 1 was lower than that at Point 2, and the Ni concentration at Point 1 was higher than that at Point 2. These results are consistent with the identification of the  $\alpha$  and  $\gamma$  phases using EPMA (Figs. 2 and 4). At Point 3, the diffraction pattern of a small bright area was identified as  $\text{Cr}_2\text{N}$  (Fig. 5e). As shown in Fig. 5a, blue areas were observed along the  $\gamma$  and  $\alpha$  phase boundary, and Point 4 in Fig. 5b represents one of the blue areas. As shown in Table 1 and Fig. 5f, Point 4 was relatively rich in Mo, and the electron diffraction pattern was considerably different from those of the  $\gamma$  (Point 1) and  $\alpha$  phases (Point 2), and was assigned to the tetragonal phase. Based on the above results, the area at Point 4 was determined to be a  $\sigma$  phase. As indicated in Table 1 and Supplementary Fig. 1, because the Mo content at Point 4 was considerably higher than in the  $\alpha$  and  $\gamma$  phases, compositional changes and  $\gamma_2$  formation may have occurred around the  $\sigma$  phases (blue areas).

To confirm the formation of  $\gamma_2$  around the  $\sigma$  phases, the electron diffraction pattern at Point 5 was obtained, and an EDS analysis was conducted. Figure 5g shows that the crystal structure of the area at Point 5 was classified as FCC, but the concentrations of Cr and Mo were lower than those of the  $\gamma$  phase at Point 1 and the  $\alpha$  phase at Point 2. Therefore, the area at Point 5 was considered to be a  $\gamma_2$  phase. In this case, Cr and Mo in the  $\gamma_2$  phase were both depleted by 2 mass% relative to the nominal composition of the UNS S32750.

This study demonstrated that the aging treatment caused  $\sigma$  phase to be formed in the  $\alpha$  and  $\gamma$  phase boundary regions, and that the  $\sigma$  phases were discolored to bluish dark-gray or blue by etching with Murakami solution (Figs. 3 and 5a). Additionally, the  $\gamma_2$  phase was thought to be formed around the  $\sigma$  phases. A comparison of Figs. 5a, b shows that the color of the  $\gamma_2$  phase did not change even after etching with Murakami solution.

### Inclusion characterization

Inclusions were observed in both the solution-treated and aged specimens. Figure 6 shows a SEM image and the corresponding EPMA maps of a S-containing inclusion in the aged specimen. As previously mentioned, inclusions existed in both the  $\alpha$  and  $\gamma$  phases, and some of them existed at the  $\alpha/\gamma$  boundaries. The inclusion shown in Fig. 6 was present at the  $\alpha$  (Cr- and Mo-rich areas) and  $\gamma$  (Ni-rich areas) phase boundary. To facilitate the comparison of the distribution of each element, the same position is indicated with white arrows on the SEM image and EDS maps. Manganese and S were detected in the upper-right part of the inclusion. Manganese, Cr, and O were detected in the left side of the inclusions. This inclusion was determined to be a Mn-Cr oxide and MnS complex. In stainless steels and related metals,  $\text{MnCr}_2\text{O}_4$  is sometimes formed, and MnS is generated at the periphery of oxide inclusions<sup>53,54</sup>. In this work, similar S-containing inclusions were observed in the solution-treated specimens. However, not all inclusions were accompanied by MnS. Approximately 500 inclusions were found in a  $2 \times 2$  mm area of the solution-treated and aged specimens (see Supplementary Table 1). The EDS analysis

**Table 1.** Relative concentrations (at.%) at Points 1, 2, 4, and 5 shown in Fig. 5b.

Point	Cr	Fe	Ni	Mo
1	26	64	7	3
2	30	62	4	4
4	31	58	4	7
5	23	69	6	2

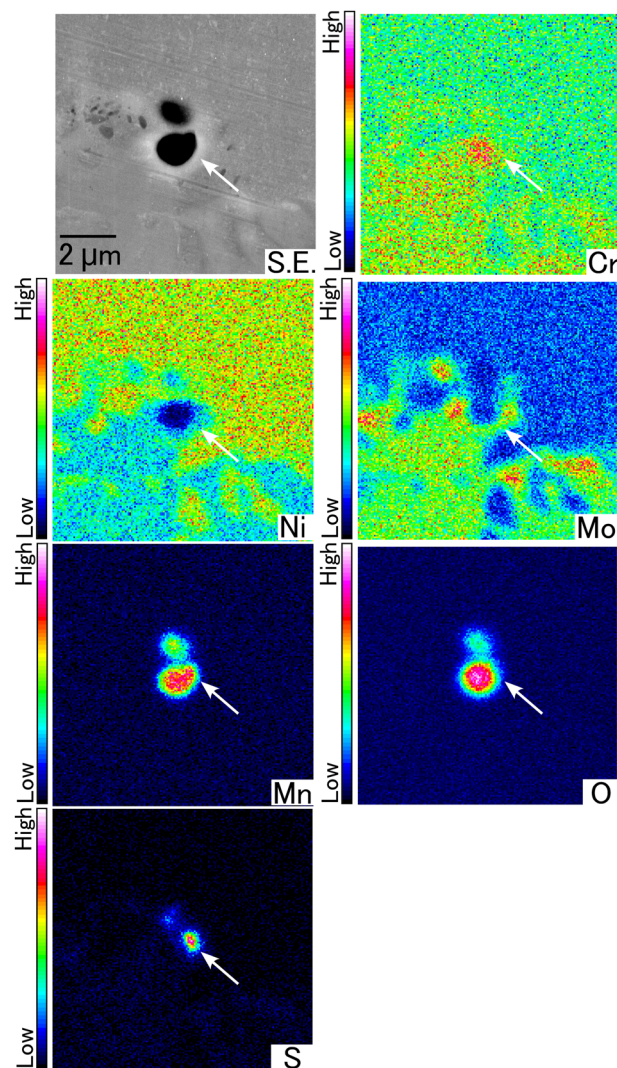


**Fig. 6 SEM image and EPMA maps.** A S-containing inclusion at an  $\alpha$  and  $\gamma$  phase boundary in the aged specimen.

was performed on the inclusions within a 2-mm square area. This analysis was performed twice for aged specimen. In both cases, one MnS-containing inclusion was confirmed to be present within the 2-mm square area. Therefore, the percentage of MnS-containing inclusions was approximately 1/500, with the remainder being simple Mn-Cr oxides. Neither the size nor the composition of inclusions changed before and after aging treatment.

### Effect of aging-treatment on the pitting corrosion resistance

Figure 7a shows the polarization curves in naturally aerated 1 M  $\text{MgCl}_2$ . The area of the working electrode was  $10 \times 10$  mm. A large

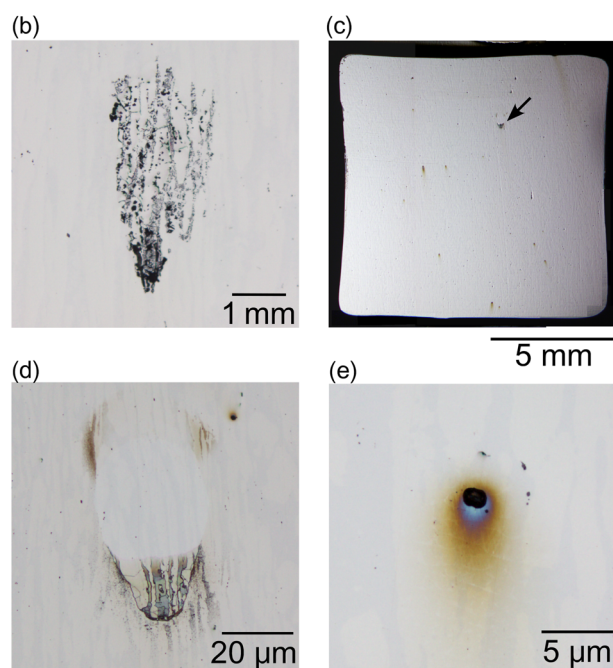
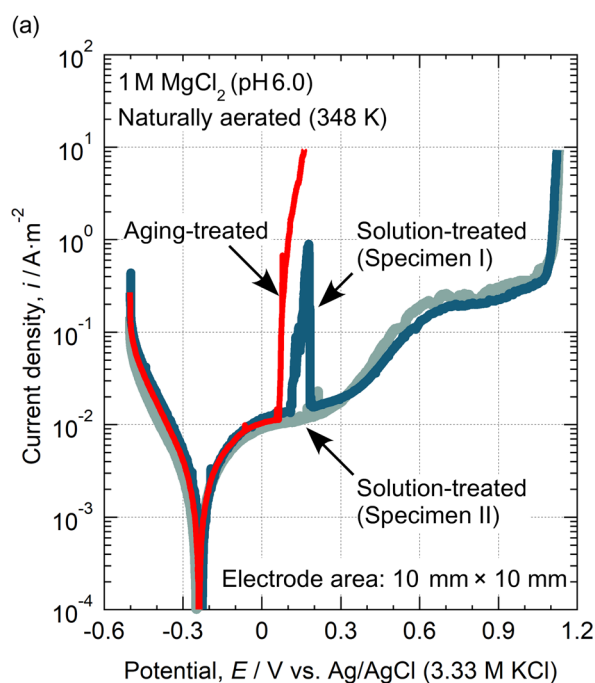


**Fig. 7 Effect of aging-treatment on the pitting corrosion resistance.** **a** Polarization curves of the solution-treated and aged specimens in naturally aerated 1 M MgCl<sub>2</sub> at pH 6.0 (348 K). Electrode area: 10 × 10 mm. **b** Optical micrograph of pitting corrosion on the aged specimen. **c** Optical micrograph of the electrode area of the solution-treated specimen (Specimen I) after polarization. **d** Enlarged view of the area indicated by the arrows in **c**. **e** Optical micrograph of localized discoloration on the solution-treated specimen (Specimen II).

increase in the anodic current of the aged specimen was observed at approximately 0.1 V due to pitting (see in Fig. 7b). In contrast, for the solution-treated specimens, there were one case where metastable pitting was observed at approximately 0.1 V (Specimen I) and one case where it was not (Specimen II). Figure 7c shows that an optical micrograph of the electrode area of the solution-treated specimen (Specimen I). After polarization,

metastable pitting corrosion was confirmed. As presented in Fig. 7d, small spots of localized discoloration were observed on both Specimens I and II, but no stable pit was initiated. The localized discoloration may have been caused by MnS-containing inclusions. The gradual increase in the current density from 0.3 to 0.6 V was due to transpassive dissolution of the steel matrix, and the large increases at approximately 1.1 V was due to oxygen evolution. For the potentiodynamic polarization of a 10 × 10 mm electrode area in 1 M MgCl<sub>2</sub>, the aged specimen was measured twice, and pitting corrosion occurred in both cases. The solution-treated specimen was measured three times, and no pitting occurred in any case. This study showed that the aging treatment at 1173 K for 1.0 ks decreases the pitting corrosion resistance of UNS S32750 super duplex stainless steel. It was also found that the  $\sigma$  and/or  $\gamma_2$  phases are essential for stable pit initiation because stable pitting did not occur on the solution-treated specimens.

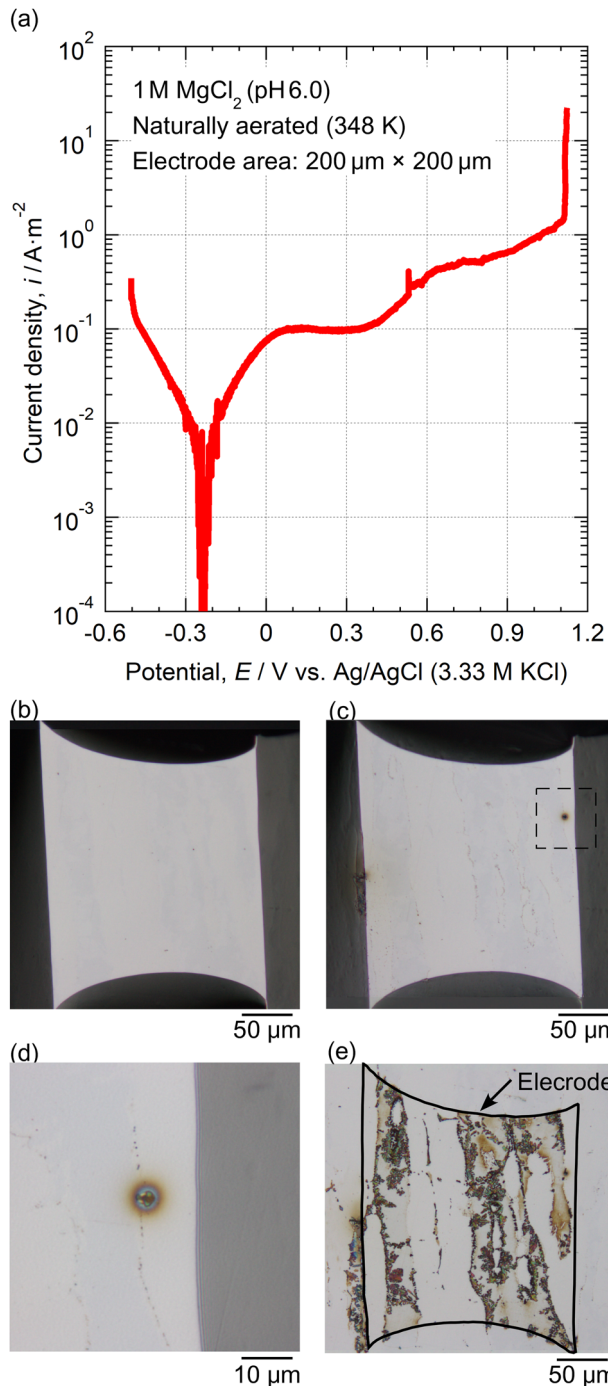
### Necessity of inclusions in pit initiation

A small electrode (200 × 200  $\mu\text{m}$ ) without inclusions was fabricated to ascertain the effect of inclusions on the pitting corrosion resistance. Figure 8a shows the polarization curve of the aged specimen in naturally aerated 1 M MgCl<sub>2</sub>, and Fig. 8b, c shows optical micrographs of the electrode surface before and after polarization, respectively. Figure 8b shows that no inclusions were visible. In this case, no stable pitting was generated, although some localized discoloration was observed after polarization (Fig. 8d). To identify the  $\alpha$ ,  $\gamma$ , and  $\sigma$  phases in the electrode area, the specimen was etched with Murakami solution after polarization. Figure 8e shows an optical micrograph after etching. This electrode area included  $\alpha$  (white areas),  $\gamma$  (brown areas), and  $\sigma$  phases (bluish dark-gray areas). The existence of  $\sigma$  phases indicates that  $\gamma_2$  phases are formed around the  $\sigma$  phases. This result indicates that the  $\sigma$  phase and/or  $\gamma_2$  phase alone cannot act as initiation sites for pitting, and some additional factors, such as inclusions, are substantial for pit initiation. As shown in Fig. 8, the small discoloration was likely to be located at the  $\alpha/\gamma$  phase boundary, and it is undeniable that this was caused by a very small inclusion. Anyway, based on the optical micrographs and polarization curves, no stable pitting was found to be generated in a small electrode area (200 × 200  $\mu\text{m}$ ) without inclusions. The potentiodynamic polarization of a small electrode without inclusions was performed five times to ascertain reproducibility. No stable pitting was generated in all cases.

### Elucidation of the pit initiation sites on the aged specimen

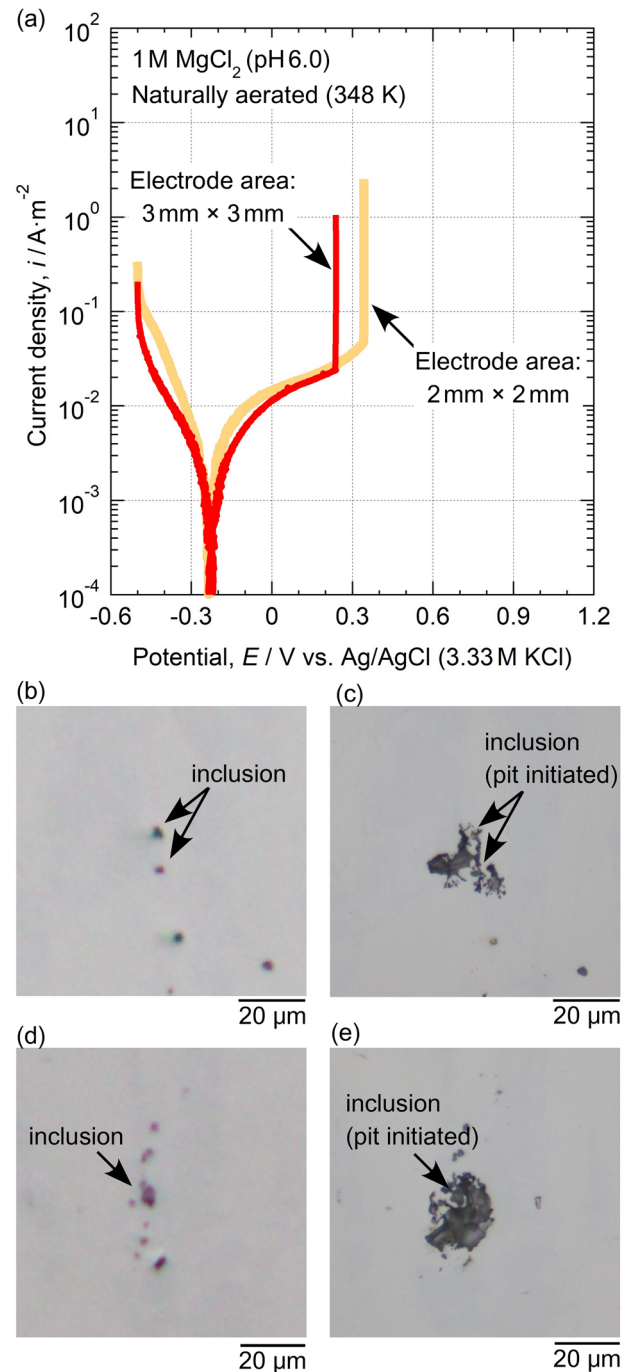
Next, the anodic polarization behavior was obtained for each location where inclusions were present, that is (1) in the  $\alpha$ , (2)  $\gamma$ , and (3)  $\gamma_2$  phases (boundary region of  $\alpha$  and  $\gamma$  phases). Also in these cases, a small electrode (200 × 200  $\mu\text{m}$ ) with an inclusion was fabricated. However, no pits occurred in either case, as shown in Supplementary Figs. 2–4. Owing to the low probability of the existence of MnS-containing inclusions, the small electrode could target Mn-Cr oxide but not MnS. Thus, larger electrodes were prepared and polarized. Figure 9a shows the polarization results of the 3 × 3 mm and 2 × 2 mm electrodes. For both cases, large increases in the anodic current density were generated. After polarization, only one pit was generated in each specimen. Figure 9b–e shows the electrode surfaces of the pit initiation sites before and after polarization. Comparing the images before and after polarization, the initiation sites of pitting were determined to be inclusions. The polarization measurements with a 3 × 3 mm electrode area were made twice, and pitting occurred in both cases. The measurements with a 2 × 2 mm electrode area were made four times, and pitting occurred in three cases.

Figure 10 shows a SEM image and the corresponding EDS maps of the pitting corrosion on the 2 × 2 mm electrode shown in Fig. 9.



**Fig. 8 Polarization behavior of a small electrode.** **a** Polarization curve of a small area ( $200 \times 200 \mu\text{m}$ ) of the aged specimen without inclusions in naturally aerated 1 M  $\text{MgCl}_2$  at pH 6.0 (348 K). **b**, **c** Optical micrographs of the electrode area **b** before and **c** after polarization. **d** Enlarged view of the area demarcated by the dashed broken square in **c**. **e** Optical micrograph of the electrode area shown in **c**.

Manganese, Cr, and O signals were detected at the center of the corroded area (pit), but no S signal was detected. The S signal was observed to be around the inclusion. This is because the S and Mo signals overlap in EDS, and the S signal was assumed to be Mo. Interestingly, the Cr and Ni EDS maps show that the inclusion and pit were present in the  $\alpha$  phase (Cr-rich area). Moreover, they were located adjacent to the  $\gamma$  phase boundary (Ni-rich region).



**Fig. 9 Polarization behavior of  $2 \times 2 \text{ mm}$  and  $3 \times 3 \text{ mm}$  electrodes.** **a** Effect of the electrode area size on the polarization behavior of the aged specimen in naturally aerated 1 M  $\text{MgCl}_2$  at pH 6.0 (348 K). **b–e** Optical micrographs of the pitting corrosion initiation sites **b**, **d** before and **c**, **e** after polarization of **b**, **c**  $2 \times 2 \text{ mm}$  and **d**, **e**  $3 \times 3 \text{ mm}$  electrodes.

As previously mentioned, the  $\sigma$  phase forms at the  $\alpha/\gamma$  phase boundaries and grows toward the  $\alpha$  phase (Fig. 3b). Thereby,  $\gamma_2$  phases were generated in the  $\alpha$  phase side of the  $\alpha/\gamma$  phase boundaries. As shown in Fig. 10, the presence of the pit in the  $\alpha$  phase suggests that the pit was initiated and grew in the  $\gamma_2$  phase, which may be due to the low corrosion resistance of the  $\gamma_2$  phase owing to the low Cr and Mo contents. In this case, no S signal was detected in the inclusion, which may be due to sulfide dissolution as a precursor to pit initiation.

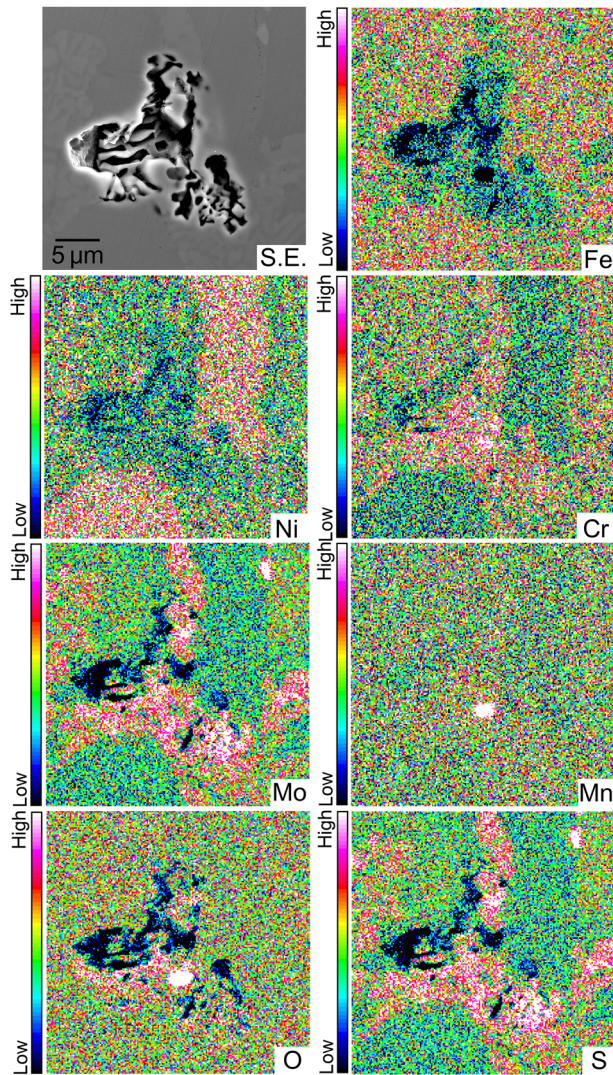


**Fig. 10** The pitting corrosion on the  $2 \times 2$  mm electrode. A SEM image of the pit shown in Fig. 9c and the corresponding EDS maps.

To observe an earlier form of pitting corrosion, potentiodynamic polarization was performed using a  $1 \times 1$  mm electrode. Figure 11a shows the polarization curve obtained in 1 M  $\text{MgCl}_2$ . Pitting corrosion was generated at 0.13 V. The measurements with a  $1 \times 1$  mm electrode area were made six times, and pitting occurred in two cases. A small electrode would be suitable for detecting the increase in current due to pitting with high sensitivity<sup>55,56</sup>. By stopping the polarization when a slight increase in current is detected, an early stage of pitting corrosion can be observed. However, as the electrode area is reduced, the probability of pit initiation decreases and the pitting potential increases abnormally<sup>57</sup>. Therefore, we conducted a number of experiments and analyzed the pit initiation site on the specimen with pitting potential close to that shown in Fig. 7 (polarization of a  $10 \times 10$  mm electrode area).

Figure 11b, c shows optical micrographs of the pitting initiation site before and after polarization shown in Fig. 11a. The pit was confirmed to be initiated at the inclusion indicated by the arrow. Figure 12 shows a SEM image and the corresponding EPMA maps of the pit initiation site. To facilitate the comparison of the elemental distributions, the same positions are indicated with black or white arrows on the SEM image and EPMA maps. In the EPMA maps, Mn, Cr, and O signals were observed in the inclusion. Additionally, although small and speckled, S was detected at the

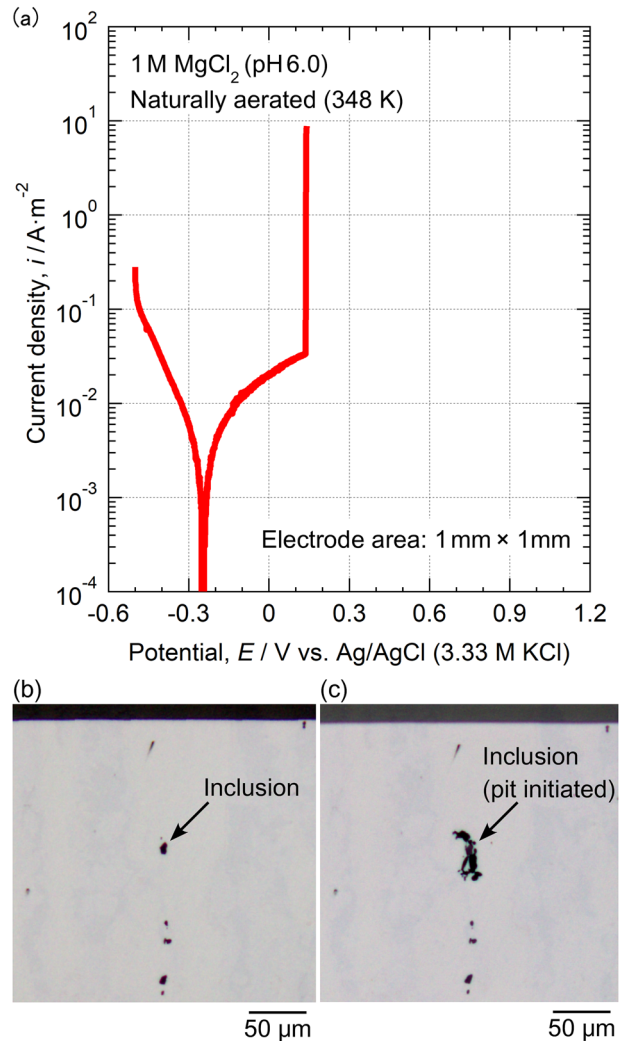


**Fig. 11** Polarization behavior of a  $1 \times 1$  mm electrode. **a** Polarization curve of a small area ( $1 \times 1$  mm) of the aged specimen with inclusions in naturally aerated 1 M  $\text{MgCl}_2$  at pH 6.0 (348 K). **b**, **c** Optical micrographs of the pitting corrosion initiation site **b** before and **c** after polarization.

point indicated by the yellow arrow. Therefore, it was determined that the pit was initiated at the Mn-Cr oxide and MnS complex inclusion. Moreover, the inclusion was located in the boundary region of the  $\alpha$  (Cr-rich region) and  $\gamma$  (Ni-rich region) phases. The Ni map shows that the inclusion and pits were located in the low-Ni region, suggesting that the inclusion was not located in the  $\gamma$  phase. Moreover, the point indicated by the black or white arrows exhibited a high Mo content and a low Cr content, which is thought to be the  $\sigma$  phase. Thus, the inclusion may be located within the  $\gamma_2$  phase adjacent to the  $\sigma$  phase. In most of the previous reports, pitting corrosion is considered to be initiated at  $\sigma$  phases. However, this study demonstrated that MnS inclusions and  $\gamma_2$  phases are important factors in the initiation of pitting corrosion on the aged UNS S32750 super duplex stainless steel.

The pitting was thought to be initiated by the synergistic effect of MnS-containing inclusions and  $\gamma_2$  phase. The MnS-containing inclusions are considered to be present in  $\alpha$  and  $\gamma$  phases as well as in  $\gamma_2$ . However, as shown in Figs. 9–12, pitting corrosion was initiated at the boundary of  $\alpha$  and  $\gamma$  phases. And,  $\gamma_2$  phases were generated in the  $\alpha$  phase side of the  $\alpha/\gamma$  phase boundaries (Fig. 5). In general, UNS S32750 super duplex stainless steel exhibits high pitting corrosion resistance due to their high Cr and Mo contents.

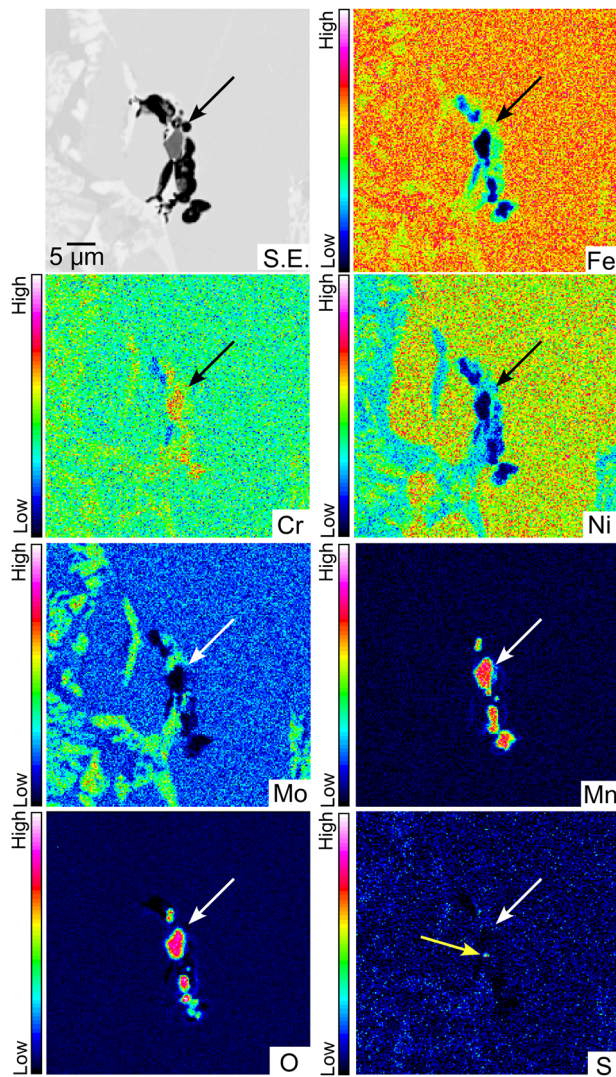


**Fig. 12** The pitting corrosion on the  $1 \times 1$  mm electrode. A SEM image of the corroded area (pit) shown in Fig. 11c and the corresponding EPMA maps. Black and white arrows indicate the same position. Yellow arrow indicates the S signal location.

However, the pitting corrosion resistance of  $\gamma_2$  phase is expected to be low due to relatively low Cr and Mo contents as shown in Table 1 (Point 5). Therefore, it is understood that pitting corrosion did not occur on the solution-treated specimen but on the aged specimen, even if MnS-containing inclusions were present (Fig. 7). Even in the case of the aged specimen, MnS-containing inclusions in  $\alpha$  and  $\gamma$  phases are not considered to be the initiation sites of pitting corrosion.

In this study, by gradually decreasing the size of the electrode area, we proposed that the initiation site of pitting corrosion on the aged specimen was MnS-containing inclusions in  $\gamma_2$  phase. In general, MnS inclusions act as the initiation sites of pitting, but no oxide-free MnS inclusions were found in the specimens used. Potentiostatic pulse technique has been proposed as a method for identifying the initiation sites of pitting corrosion on stainless steels<sup>23,58,59</sup>. Similarly, the method used in this study of varying the electrode area may also be effective.

The following is a summary of this study.

1. An aging treatment of UNS S32750 super duplex stainless steel at 1173 K for 1.0 ks produced  $\sigma$  and  $\gamma_2$  phases in the  $\alpha$  and  $\gamma$  phase boundary regions. Mn-Cr oxide and MnS

**Table 2.** Chemical composition of the duplex stainless steel (mass%).

C	Si	Mn	P	S	Ni	Cr	Mo	N
0.017	0.32	0.50	0.02	0.0006	7.00	25.1	4.01	0.29

complex inclusions were present in the steel; however, not all oxide inclusions were accompanied by MnS.

2. No stable pitting occurred on the solution-treated specimen during potentiodynamic polarization in 1 M  $\text{MgCl}_2$  at 348 K (electrode area:  $10 \times 10$  mm), but pitting corrosion was initiated on the aged specimen at approximately 0.1 V.
3. No pitting was observed on the aged specimen during the potentiodynamic polarization of a small area ( $200 \times 200 \mu\text{m}$ ) without inclusions in 1 M  $\text{MgCl}_2$  at 348 K. Because the electrode area was thought to include  $\alpha$ ,  $\gamma$ ,  $\sigma$ , and  $\gamma_2$  phases, the  $\sigma$  phase and/or  $\gamma_2$  phase alone could not act as the pitting initiation sites.
4. Potentiodynamic polarization was performed on the aged specimen using a  $1 \times 1$  mm electrode in 1 M  $\text{MgCl}_2$  at 348 K. A stable pit was initiated at approximately 0.15 V at the inclusion located in the  $\alpha$  and  $\gamma$  phase boundary region. Based on the EPMA analysis, the initiation site was concluded to be a MnS-containing Mn-Cr oxide inclusion in the  $\gamma_2$  phase.

## METHODS

### Specimens and electrolyte

A 20 mm-thick hot-rolled UNS S32750 super-duplex stainless steel plate was used as the specimen in this study. Table 2 presents the chemical composition of the steel, which shows that the S concentration in the steel was very low (0.0006 mass %). Two types of heat treatment were performed, namely a (1) solution treatment and (2) aging treatment. The solution treatment was performed at 1373 K for 1.8 ks (water-quenched). After the solution treatment, an isothermal aging treatment was conducted at 1173 K for 1.0 ks (water-quenched). Subsequently, the steel plate was cut into  $15 \times 25 \times 5$  mm coupons. The specimens were mechanically ground with SiC paper to 1500 grit and then polished with successive diamond suspensions of 6 and 1  $\mu\text{m}$ . Finally, the specimens were ultrasonically cleaned using ethanol.

A 1 M  $\text{MgCl}_2$  solution was used as the electrolyte for the polarization measurements. The pH of the solution was adjusted to 6.0 using  $\text{Mg}(\text{OH})_2$ . The solution was prepared using deionized water and analytical-grade chemicals. In the evaluation of stress corrosion cracking (SCC) of stainless steels,  $\text{MgCl}_2$  is often used. To extend this study to SCC studies,  $\text{MgCl}_2$  was used as an electrolyte.

### Polarization measurements

Potentiodynamic polarization measurements were conducted in a naturally aerated 1 M  $\text{MgCl}_2$  solution at 348 K. Different working electrode areas of different sizes were used, namely (1)  $10 \times 10$  mm, (2)  $3 \times 3$  mm, (3)  $2 \times 2$  mm, (4)  $1 \times 1$  mm, and (5)  $200 \times 200 \mu\text{m}$ . The area was accurately measured after polarization, and the current was converted to current density. The electrode areas were fabricated using resin. A battery-powered potentiostat was used to reduce the electrical noise when the electrode area was  $200 \times 200 \mu\text{m}^2$ . The conventional three-electrode method was used for all the polarization measurements. The electrode potential scan rate was  $23 \text{ mV min}^{-1}$ . The counter electrode was a Pt sheet and the reference electrode was Ag/AgCl (3.33 M KCl). The temperature of the reference electrode was 298 K, and all electrode potentials in this study refer to the Ag/AgCl (3.33 M KCl) electrode at 298 K.



## Surface and cross-sectional observations

Chemical etching in a 10% NaOH-0.1%  $K_3Fe(CN)_6$  solution, also known as the Murakami solution, was performed for 90 min at 298 K for metallographic examination. Optical microscopy and field-emission scanning electron microscopy (SEM) equipped with an energy-dispersive X-ray spectroscopy (EDS) system were used to observe the specimen surfaces. An acceleration voltage of 20 kV was used for the SEM observation and EDS analysis. In general, it is difficult to distinguish the S and Mo EDS signals. An electron probe microanalyzer (EPMA) was used to separate Mo and S signals. The electron acceleration voltage was set to 15 kV. A focused ion beam (FIB) system and scanning transmission electron microscopy (STEM) were used to observe the phase boundary regions. The FIB lift-out specimens were fabricated using a Ga ion beam. The accelerating voltage for the STEM observations was 200 kV.

## DATA AVAILABILITY

The datasets generated during and/or analyzed during the current study are available from the corresponding author on reasonable request.

Received: 10 November 2022; Accepted: 21 February 2023;

Published online: 04 March 2023

## REFERENCES

- Kong, D., Dong, C., Ni, X. & Li, X. Corrosion of metallic materials fabricated by selective laser melting. *npj Mater. Degrad.* **3**, 24 (2019).
- Saito, H., Muto, I., Nishimoto, M. & Sugawara, Y. Corrosion-resistant sintered stainless steels with non-equilibrium Mo-rich phases. *Mater. Today Commun.* **33**, 104211 (2022).
- Davison, R. M. & Redmond, J. D. A guide to using duplex stainless steels. *Mater. Design* **12**, 187–192 (1991).
- Voronenko, B. I. Austenitic-ferritic stainless steels: a state-of-the-art review. *Met. Sci. Heat Treat.* **39**, 428–437 (1997).
- Nilsson, J.-O. Super duplex stainless steels. *Mater. Sci. Technol.* **8**, 685–700 (1992).
- Chail, G. & Kangas, P. Super and hyper duplex stainless steels: structures, properties and applications. *Procedia Struct. Integr.* **2**, 1755–1762 (2016).
- George, P. et al. Machinability, weldability and surface treatment studies of SDSS 2507 material-A review. *Mater. Today Proc.* **46**, 7682–7687 (2021).
- Wilms, M. E., Gadgil, V. J., Krougman, J. M. & Ijsseling, F. P. The effect of  $\sigma$ -phase precipitation at 800°C on the corrosion resistance in sea-water of a high alloyed duplex stainless steel. *Corros. Sci.* **36**, 871–881 (1994).
- Zou, D., Han, Y., Zhang, W. & Yu, J. Sigma phase precipitation and properties of super-duplex stainless steel UNS S32750 aged at the nose temperature. *J. Wuhan Univ. Technol.-Mat. Sci. Edit.* **26**, 182–185 (2011).
- Moon, I.-J., Jang, B.-S. & Koh, J.-H. Heat treatment effect on pitting corrosion of super duplex stainless steel UNS S32750 GTA welds. *Adv. Mat. Res.* **746**, 467–472 (2013).
- Pardal, J. M. et al. Influence of the grain size on deleterious phase precipitation in superduplex stainless steel UNS S32750. *Mater. Charact.* **60**, 165–172 (2009).
- Wang, R. Precipitation of sigma phase in duplex stainless steel and recent development on its detection by electrochemical potentiokinetic reactivation: a review. *Corros. Commun.* **2**, 41–54 (2021).
- Sato, Y. S. & Kokawa, H. Preferential precipitation site of sigma phase in duplex stainless steel weld metal. *Scr. Mater.* **40**, 659–663 (1999).
- Chen, T. H. & Yang, J. R. Effects of solution treatment and continuous cooling on  $\sigma$ -phase precipitation in a 2205 duplex stainless steel. *Mater. Sci. Eng. A* **311**, 28–41 (2001).
- Martins, M. & Casteletti, L. C. Heat treatment temperature influence on ASTM A890 GR 6A super duplex stainless steel microstructure. *Mater. Charact.* **55**, 225–233 (2005).
- Elmer, J. W., Palmer, T. A. & Specht, E. D. Direct observations of sigma phase formation in duplex stainless steels using in-situ synchrotron X-ray diffraction. *Metall. Mater. Trans. A* **38**, 464–475 (2007).
- Martins, M. & Casteletti, L. C. Sigma phase morphologies in cast and aged super duplex stainless steel. *Mater. Charact.* **60**, 792–795 (2009).
- Hsieh, C.-C. & Wu, W. Overview of intermetallic sigma ( $\sigma$ ) phase precipitation in stainless steels. *Int. Sch. Res. Notices* **2012**, 732471 (2012).
- Chan, K. W. & Tjong, S. C. Effect of secondary phase precipitation on the corrosion behavior of duplex stainless steels. *Materials* **7**, 5268–5304 (2014).
- Marques, I. J., Vicente, A. A., Tenório, J. A. S. & Santos, T. F. A. Double kinetics of intermetallic phase precipitation in UNS S32205 duplex stainless steels submitted to isothermal heat treatment. *Mater. Res.* **20**, 152–158 (2017).
- Silva, D. D. S. et al. Microstructural influence of sigma phase on pitting corrosion behavior of duplex stainless steel/NaCl electrolyte couple. *Mater. Chem. Phys.* **259**, 124056 (2021).
- Sriram, R. & Tromans, D. Pitting corrosion of duplex stainless steels. *Corrosion* **45**, 804–810 (1989).
- Gao, J., Jiang, Y., Deng, B., Ge, Z. & Li, J. Determination of pitting initiation of duplex stainless steel using potentiostatic pulse technique. *Electrochim. Acta* **55**, 4837–4844 (2010).
- Santos, D. C., Magnabosco, R. & Moura-Neto, C. Influence of sigma phase formation on pitting corrosion of an aged UNS S31803 duplex stainless steel. *Corrosion* **69**, 900–911 (2013).
- Guo, Y. et al. Microstructure evolution and pitting corrosion resistance of the Gleeble-simulated heat-affected zone of a newly developed lean duplex stainless steel 2002. *J. Alloys Compd.* **658**, 1031–1040 (2016).
- He, L., Wirian, L. & Singh, P. M. Effects of isothermal aging on the microstructure evolution and pitting corrosion resistance of lean duplex stainless steel UNS S32003. *Metall. Mater. Trans. A* **50**, 2103–2113 (2019).
- Pak, S. & Karlsson, L. Optimizing the properties of duplex stainless weld metals by addition of nitrogen. *Scand. J. Metall.* **19**, 9–13 (1990).
- Nilsson, J. O. & Wilson, A. Influence of isothermal phase transformations on toughness and pitting corrosion of super duplex stainless steel SAF 2507. *Mater. Sci. Technol.* **9**, 545–554 (1993).
- Nilsson, J.-O., Karlsson, L. & Andersson, J.-O. Secondary austenite formation and its relation to pitting corrosion in duplex stainless steel weld metal. *Mater. Sci. Technol.* **11**, 276–283 (1995).
- Kobayashi, D. Y. & Wolynec, S. Evaluation of the low corrosion resistant phase formed during the sigma phase precipitation in duplex stainless steels. *Mater. Res.* **2**, 239–247 (1999).
- Deng, B. et al. Evaluation of localized corrosion in duplex stainless steel aged at 850°C with critical pitting temperature measurement. *Electrochim. Acta* **54**, 2790–2794 (2009).
- Kumar, B. S. & Kain, V. Macro and micro electrochemical techniques to study influence of sigma phase formation in a duplex stainless steel. *Adv. Mater. Res.* **794**, 583–591 (2013).
- Park, C. J., Rao, V. S. & Kwon, H. S. Effects of sigma phase on the initiation and propagation of pitting corrosion of duplex stainless steel. *Corrosion* **61**, 76–83 (2005).
- Pardal, J. M. et al. Deleterious phases precipitation on superduplex stainless steel UNS S32750: characterization by light optical and scanning electron microscopy. *Mater. Res.* **13**, 401–407 (2010).
- Cojocar, E. M., Raducanu, D., Nocivin, A. & Cojocar, V. D. Influence of ageing treatment temperature and duration on  $\sigma$ -phase precipitation and mechanical properties of UNS S32750 SDSS alloy. *J. Adv. Res.* **30**, 53–61 (2021).
- Zhang, B. et al. Precipitation behavior and phase transformation of hyper duplex stainless steel UNS S32707 at nose temperature. *Mater. Charact.* **129**, 31–39 (2017).
- Suter, T., Webb, E. G., Böhni, H. & Alkire, R. C. Pit initiation on stainless steels in 1 M NaCl with and without mechanical stress. *J. Electrochem. Soc.* **148**, B174–B185 (2001).
- Webb, E. G., Suter, T. & Alkire, R. C. Microelectrochemical measurements of the dissolution of single MnS inclusions, and the prediction of the critical conditions for pit initiation on stainless steel. *J. Electrochem. Soc.* **148**, B186–B195 (2001).
- Muto, I., Ito, D. & Hara, N. Microelectrochemical investigation on pit initiation at sulfide and oxide inclusions in type 304 stainless steel. *J. Electrochem. Soc.* **156**, C55–C61 (2009).
- Chiba, A., Muto, I., Sugawara, Y. & Hara, N. A Microelectrochemical system for in situ high-resolution optical microscopy: morphological characteristics of pitting at MnS inclusion in stainless steel. *J. Electrochem. Soc.* **159**, C341–C350 (2012).
- Chiba, A., Muto, I., Sugawara, Y. & Hara, N. Pit initiation mechanism at MnS inclusions in stainless steel: synergistic effect of elemental sulfur and chloride ions. *J. Electrochem. Soc.* **160**, C511–C520 (2013).
- Nishimoto, M., Muto, I., Sugawara, Y. & Hara, N. Morphological characteristics of trenching around MnS inclusions in type 316 stainless steel: the role of molybdenum in pitting corrosion resistance. *J. Electrochem. Soc.* **166**, C3081–C3089 (2019).
- Nishimoto, M., Muto, I., Sugawara, Y. & Hara, N. Passivity of (Mn,Cr)S inclusions in type 304 stainless steel: The role of Cr and the critical concentration for preventing inclusion dissolution in NaCl solution. *Corros. Sci.* **176**, 109060 (2020).
- Tokuda, S., Muto, I., Sugawara, Y. & Hara, N. Effect of sensitization on pitting corrosion at MnS and CrS in type 304 stainless steel. *J. Electrochem. Soc.* **168**, 091504 (2021).

45. Liu, P., Zhang, Q. H., Watanabe, Y., Shoji, T. & Cao, F.-H. A critical review of the recent advances in inclusion-triggered localized corrosion in steel. *npj Mater. Degrad.* **6**, 81 (2022).
46. Duan, Z., Man, C., Cui, H., Cui, Z. & Wang, X. Formation mechanism of MnS inclusion during heat treatments and its influence on the pitting behavior of 316L stainless steel fabricated by laser powder bed fusion. *Corros. Commun.* **7**, 12–22 (2022).
47. Takayama, R., Nishimoto, M., Muto, I. & Sugawara, Y. Micro-electrochemical aspects of the effects of temperature on pit initiation at MnS inclusion in type 304 stainless steel. *J. Electrochem. Soc.* **169**, 111501 (2022).
48. Garfias, L. F. & Siconolfi, D. J. In situ high-resolution microscopy on duplex stainless steels. *J. Electrochem. Soc.* **147**, 2525–2531 (2000).
49. Yang, Y., Yan, B., Li, J. & Wang, J. The effect of large heat input on the microstructure and corrosion behaviour of simulated heat affected zone in 2205 duplex stainless steel. *Corros. Sci.* **53**, 3756–3763 (2011).
50. Zhang, Z., Zhao, H., Zhang, H., Hu, J. & Jin, J. Microstructure evolution and pitting corrosion behavior of UNS S32750 super duplex stainless steel welds after short-time heat treatment. *Corros. Sci.* **121**, 22–31 (2017).
51. Otake, A., Muto, I., Chiba, A., Sugawara, Y. & Hara, N. Pitting at the  $\delta/\gamma$  boundary of type 304 stainless steel in NaCl solution: the role of oxide inclusions and segregation. *J. Electrochem. Soc.* **164**, C991–C1002 (2019).
52. Putz, A. et al. Methods for the measurement of ferrite content in multipass duplex stainless steel welds. *Weld World* **63**, 1075–1086 (2019).
53. Zheng, S. J. et al. Identification of MnCr<sub>2</sub>O<sub>4</sub> nano-octahedron in catalysing pitting corrosion of austenitic stainless steels. *Acta Mater.* **58**, 5070–5085 (2010).
54. Pao, L., Muto, I. & Sugawara, Y. Pitting at inclusions of the equiatomic CoCr-FeMnNi alloy and improving corrosion resistance by potentiodynamic polarization in H<sub>2</sub>SO<sub>4</sub>. *Corros. Sci.* **191**, 109748 (2021).
55. Tokuda, S., Muto, I., Sugawara, Y. & Hara, N. The role of applied stress in the anodic dissolution of sulfide inclusions and pit initiation of stainless steels. *Corros. Sci.* **183**, 109312 (2021).
56. Tokuda, S., Muto, I., Sugawara, Y. & Hara, N. High-temperature heat-treatment at 1673 K: improvement of pitting corrosion resistance at inclusions of type 304 stainless steel under applied stress. *Mater. Trans.* **63**, 265–268 (2022).
57. Burstein, G. T. & Ilevbare, G. O. The effect of specimen size on the measured pitting potential of stainless steel. *Corros. Sci.* **38**, 2257–2265 (1996).
58. Chen, B. et al. Use of the potentiostatic pulse technique to study and influence pitting behavior of 317L stainless steel. *J. Electrochem. Soc.* **167**, 041509 (2020).
59. Tan, X. et al. Roles of different components of complex inclusion in pitting of 321 stainless steel: Induction effect of CaS and inhibition effect of TiN. *Corros. Sci.* **209**, 110692 (2022).
60. Muto, I., Izumiyama, Y. & Hara, N. Microelectrochemical measurements of dissolution of mns inclusions and morphological observation of metastable and stable pitting on stainless steel. *J. Electrochem. Soc.* **154**, C439–C444 (2007).

## ACKNOWLEDGEMENTS

This study was supported by JSPS KAKENHI Grants Numbers JP21K18804 and JP22H00254 from the Japanese Society for the Promotion of Science. Part of this

study was conducted at the Research Center for Rare Metal and Green Innovation (RaMGI), Tohoku University, which was established with the support of the Ministry of Economy, Trade, and Industry (METI) and the Ministry of Education, Culture, Sports, Science, and Technology (MEXT).

## AUTHOR CONTRIBUTIONS

S.A.: Investigation, methodology, data curation, visualization, Writing—original draft, funding acquisition. M.N.: Methodology, writing—review and editing. I.M.: Conceptualization, methodology, writing—review and editing, supervision, funding acquisition. M.K.: Resources, funding acquisition. Y.T.: Resources, funding acquisition. Y.S.: Writing—review and editing.

## COMPETING INTERESTS

The authors declare no competing interests.

## ADDITIONAL INFORMATION

**Supplementary information** The online version contains supplementary material available at <https://doi.org/10.1038/s41529-023-00335-8>.

**Correspondence** and requests for materials should be addressed to Shuichiro Amatsuka or Izumi Muto.

**Reprints and permission information** is available at <http://www.nature.com/reprints>

**Publisher's note** Springer Nature remains neutral with regard to jurisdictional claims in published maps and institutional affiliations.



**Open Access** This article is licensed under a Creative Commons Attribution 4.0 International License, which permits use, sharing, adaptation, distribution and reproduction in any medium or format, as long as you give appropriate credit to the original author(s) and the source, provide a link to the Creative Commons license, and indicate if changes were made. The images or other third party material in this article are included in the article's Creative Commons license, unless indicated otherwise in a credit line to the material. If material is not included in the article's Creative Commons license and your intended use is not permitted by statutory regulation or exceeds the permitted use, you will need to obtain permission directly from the copyright holder. To view a copy of this license, visit <http://creativecommons.org/licenses/by/4.0/>.

© The Author(s) 2023